

# High-fidelity stellar extinction with *Gaia* and APOGEE – I. The method and a new extinction curve

Jie Yu<sup>1,2,3,4\*</sup>, Luca Casagrande<sup>4</sup>, John A. Taylor<sup>3</sup>, Ioana Ciucă<sup>5</sup>, Giacomo Cordini<sup>4</sup>, Ronald Drimmel<sup>6</sup>, Shourya Khanna<sup>6</sup>, Hiep Nguyen<sup>4</sup>, Tomasz Różański<sup>4,7</sup>, Dennis Stello<sup>8,9</sup>, Haibo Yuan<sup>10,11</sup>, Zhen Yuan<sup>1,2</sup>

<sup>1</sup> School of Astronomy and Space Science, Nanjing University, Nanjing 210023, People's Republic of China

<sup>2</sup> Key Laboratory of Modern Astronomy and Astrophysics, Ministry of Education, Nanjing 210023, People's Republic of China

<sup>3</sup> School of Computing, Australian National University, Acton, ACT 2601, Australia

<sup>4</sup> Research School of Astronomy & Astrophysics, Australian National University, Cotter Rd., Weston, ACT 2611, Australia

<sup>5</sup> Kavli Institute for Particle Astrophysics & Cosmology (KIPAC), Stanford University, Stanford, CA 94305, USA

<sup>6</sup> INAF - Osservatorio Astrofisico di Torino, via Osservatorio 20, 10025 Pino Torinese (TO), Italy

<sup>7</sup> Astronomical Institute, University of Wrocław, Kopernika 11, 51-622 Wrocław, Poland

<sup>8</sup> School of Physics, University of New South Wales, Sydney, NSW 2052, Australia

<sup>9</sup> Sydney Institute for Astronomy, School of Physics, A28, The University of Sydney, NSW 2006, Australia

<sup>10</sup> Institute for Frontiers in Astronomy and Astrophysics, Beijing Normal University, Beijing 102206, People's Republic of China

<sup>11</sup> School of Physics and Astronomy, Beijing Normal University, No. 19 Xinjiekouwai St., Haidian District, Beijing 100875, People's Republic of China

Accepted XXX. Received YYY; in original form ZZZ

## ABSTRACT

The scarcity of high-fidelity extinction measurements remains a bottleneck in deriving accurate stellar properties from *Gaia* parallaxes. In this work, we aim to derive precision extinction estimates for APOGEE DR19 stars, establishing a new benchmark for Galactic stellar population studies. We first determine reddening by comparing observed colors—retrieved from photometric surveys or standardized synthetic magnitudes from *Gaia* BP/RP spectra—to intrinsic colors predicted via an XGBoost model. The model is trained on minimally reddened stars to infer intrinsic colors and their associated uncertainties, using APOGEE stellar parameters ( $T_{\text{eff}}$ ,  $\log g$ , [Fe/H], and  $[\alpha/\text{Fe}]$ ). The derived reddening values are then converted into extinctions using an anchor ratio of  $A_{\text{BP}}/A_{\text{RP}} = 1.694 \pm 0.004$ , derived from red-clump-like stars. Here, we provide extinction measurements in 39 filters across 10 photometric systems and introduce a new empirical extinction curve optimized for broadband passbands. Our extinction estimates ( $A_V$ ) outperform existing results (Bayestar19, StarHorse, SEDEX), achieving a typical precision of  $\sim 0.03$  mag in  $A_V$ . Notably, we identify systematic deviations of up to 30% between monochromatic and passband-integrated extinction ratios at wavelengths  $\lambda > 700$  nm. This result highlights the necessity of adopting passband-specific coefficients when correcting extinction to derive stellar parameters. As the foundation for a forthcoming series of papers, these benchmark measurements will be used to (1) revise asteroseismic scaling relations, (2) calibrate differential reddening in open clusters, and (3) reconcile heterogeneous dust maps into a unified, all-sky extinction scheme.

**Key words:** (ISM:) dust, extinction – stars: fundamental parameters – techniques: photometric

## 1 INTRODUCTION

The release of trigonometric parallaxes for 1.5 billion stars in *Gaia* DR3 (Lindegren et al. 2021) has fundamentally transformed stellar astrophysics, enabling stellar properties (e.g., luminosity, radius, and age) to be inferred on unprecedented Galactic scales. These quantities in turn underpin exoplanet characterization, stellar evolution modeling, and chemo-dynamical studies of the Milky Way. However, the accuracy of these inferred parameters is fundamentally limited by interstellar extinction. Extinction, which reflects the wavelength-dependent absorption and scattering of starlight by dust grains, must be accurately accounted for before parallaxes can be re-

liably translated into physical properties. Extinction amplitude varies significantly with environment, sightline, and Galactic position (e.g., Green et al. 2019; Lallement et al. 2022; Wang et al. 2025b). Consequently, imprecise or inaccurate extinction corrections remain a key source of uncertainty in precision astrophysics.

To mitigate this fundamental limitation, high-fidelity, star-by-star extinction measurements are urgently required across diverse dust environments, from the local neighborhood to the highly obscured Galactic bulge. Despite intensive efforts, such precise measurements remain scarce. The APOGEE DR19 release of spectroscopy provides a timely opportunity to address this gap, owing to its precise stellar parameters ( $T_{\text{eff}}$ ,  $\log g$ , [Fe/H], and  $[\alpha/\text{Fe}]$ ) for nearly one million stars (Mészáros et al. 2025). In this work, we prioritise APOGEE data because of its high quality and homogeneity, as

\* E-mail: jie.yu@nju.edu.cn (NNU)

incorporating spectroscopic data from other surveys introduce systematic inconsistencies (Yu et al. 2023). These stellar parameters allow us to empirically establish the intrinsic colors of stars using nearby, minimally-reddened stars as a training sample. For more distant stars, their intrinsic colors can then be robustly inferred from their spectroscopic properties. The difference between the observed color and this predicted intrinsic color yields the color excess, which subsequently can be converted into extinction values assuming an extinction curve (Wang & Chen 2019). This technique, often referred to as the star-pair method (Stecher 1965; Massa et al. 1983; Yuan et al. 2013; Wang et al. 2025b), has been widely and successfully applied for extinction and reddening determinations across many large photometric surveys (e.g., Yuan et al. 2013; Wang & Chen 2019; Zhang & Yuan 2023), such as SDSS (Alam et al. 2015), Pan-STARRS (Chambers et al. 2019), and 2MASS (Cutri et al. 2003).

For the precise determination of stellar reddening and extinction, our methodology leverages the high precision of the APOGEE DR19 stellar parameters. However, APOGEE’s spectroscopic footprint primarily lies in the northern hemisphere (SDSS Collaboration et al. 2025), leading to substantially reduced overlap with major southern photometric surveys (e.g., SkyMapper, Onken et al. 2019, 2024). A transformative development that addresses this limitation comes from the availability of *Gaia* BP/RP spectrophotometry (De Angeli et al. 2023). *Gaia* DR3 delivers flux- and wavelength-calibrated spectrophotometry for roughly 220 million sources, continuously spanning 330 to 1050 nm. From these spectra, synthetic magnitudes can be generated for virtually any passband within this wavelength interval (Gaia Collaboration et al. 2023a; De Angeli et al. 2023; Montegriffo et al. 2023). Crucially, *Gaia* provides standardized synthetic photometry that is externally calibrated using standard stars, achieving the precision and internal consistency required for robust extinction measurements across diverse filter systems (Gaia Collaboration et al. 2023a). By utilizing this standardized photometry, we mitigated residual systematics that may persist in the BP/RP spectra despite official corrections (Huang et al. 2024), as previously noted by the *Gaia* collaboration (Montegriffo et al. 2023). Thus, even where direct broadband photometry is significantly incomplete within APOGEE’s footprint, the combination of APOGEE stellar parameters and standardized *Gaia* BP/RP synthetic magnitudes allows us to generate homogeneous, cross-survey magnitudes and, in turn, produce consistent extinction catalogues for many photometric systems.

As the first paper in this series, this study focuses on the derivation of high-fidelity, star-by-star extinction values for APOGEE stars and the construction of a new empirical extinction curve optimized for broadband passbands. The extinction curve describes how interstellar dust dims starlight as a function of wavelength ( $\lambda$ ), usually expressed as the ratio  $A_\lambda/A_V$ , where  $A_V$  serves as the reference extinction, though more recent parameterizations of the extinction curve have favored the monochromatic extinction at 550nm as the reference extinction. Furthermore, the profile of the extinction curve varies along different lines of sight, driven by dust properties, such as grain size and composition (Green et al. 2025). Historically, it has been assumed that extinction curves can be represented as a family of profiles, with their overall characteristics primarily determined by  $R_V \equiv A_V/E(B-V)$ , the ratio of total-to-selective extinction (Cardelli et al. 1989; Fitzpatrick 1999; Gordon et al. 2023). This ratio  $R_V$  varies significantly across the Milky Way (Peek & Schiminovich 2013; Zhang et al. 2023; Green et al. 2025; Drimmel et al. 2026). In diffuse interstellar regions it is typically  $R_V \approx 3.1$ , but it can increase to  $R_V \approx 5$  or higher in the core region of dense molecular clouds,

and can be as low as  $R_V \approx 2.5$  toward high latitudes of the Milky Way.

Previous studies have provided canonical extinction curves across various wavelength ranges. Those include the far-ultraviolet (FUV) from 912 to 1190 Å (Gordon et al. 2009), the optical from 0.3 to 1  $\mu\text{m}$  (Fitzpatrick et al. 2019), the near-infrared (NIR) from 0.8 to 5.5  $\mu\text{m}$  (Decleir et al. 2022), and the mid-infrared (MIR) from 5 to 32  $\mu\text{m}$  (Gordon et al. 2021), as well as a comprehensive extinction curve spanning the full spectral range (Gordon et al. 2023). However, because these canonical extinction curves are defined monochromatically ( $A_\lambda$ ), simply applying them directly to a broadband filter by interpolating to the (weighted-mean) effective wavelength of the filter may introduce significant biases. This simplification ignores the intricate interplay between the full stellar spectral energy distribution (SED), the detailed extinction curve  $A_\lambda$ , the filter transmission profile  $\Theta_\zeta(\lambda)$ , and the bandpass width ( $\lambda_1 - \lambda_2$ ). The correct extinction for a filter  $\zeta$  should instead be computed as:

$$A_\zeta = -2.5 \log \left( \frac{\int_{\lambda_1}^{\lambda_2} 10^{-0.4 A_\lambda} F_\lambda \Theta_\zeta(\lambda) d\lambda}{\int_{\lambda_1}^{\lambda_2} F_\lambda \Theta_\zeta(\lambda) d\lambda} \right), \quad (1)$$

which properly accounts for the shape of the stellar spectrum  $F_\lambda$ , the extinction curve  $A_\lambda$ , and the filter response over the entire passband. In this work, we aim to derive a new empirical extinction curve expressed in terms of  $A_\zeta/A_V$  for a variety of photometric bands  $\zeta$ . By using stars that span a wide range in effective temperature, metallicity, and extinction — and by directly measuring extinction in each band from observations — we avoid the simplifying assumptions inherent in applying a fixed, monochromatic extinction curve onto broadband systems. The result is a set of empirically-grounded, band-specific reddening and extinction coefficients averaged over spectral types, which are valuable for deriving intrinsic stellar parameters from observed colours and magnitudes.

Along with this new empirical extinction curve, these precise extinction measurements open the door to several significant scientific applications. Following this first paper in the series, our results will facilitate a revision of the asteroseismic scaling relation for the frequency of maximum power ( $\nu_{\text{max}}$ , Brown et al. 1991; Kjeldsen & Bedding 1995, which is known to be affected by systematic biases (Hekker 2020). Since the scaling relations for  $\nu_{\text{max}}$  and the large frequency separation ( $\Delta\nu$ , Ulrich 1986) are fundamental for inferring stellar properties such as luminosity (Yu et al. 2016, 2020), they can be used in conjunction with bolometric corrections to derive extinctions and distances (Rodrigues et al. 2014). Our independent extinction measurements, therefore, provide a direct benchmark to test and calibrate the  $\nu_{\text{max}}$  scaling relation. Beyond asteroseismology, our extinction framework can be applied to provide anchor points for the robust absolute calibration of the differential reddening of open clusters (Kalup & Molnár 2026), enabling more reliable age determinations from isochrone fitting. Finally, by exploiting high-precision extinction measurements along many lines of sight, we can reconcile heterogeneous dust-map products (e.g., Drimmel et al. 2003; Marshall et al. 2006; Sale et al. 2014; Green et al. 2019; Lallement et al. 2022) into a single, homogeneous, and continuous extinction scheme, yielding a unified catalog of the Milky Way that supports a broad range of stellar, Galactic, and interstellar-medium studies.

## 2 DATA

### 2.1 Stellar parameters in APOGEE DR19

The Apache Point Observatory Galactic Evolution Experiment (APOGEE), part of the Sloan Digital Sky Survey (SDSS), is a large-scale spectroscopic survey designed to obtain high-resolution, near-infrared spectra of stars (Majewski et al. 2017). APOGEE spectra have a resolution of  $R \sim 22,500$  and cover the H-band (1.51–1.69  $\mu\text{m}$ ), which minimizes interstellar extinction and enables the study of stars in highly obscured Galactic regions (Wilson et al. 2019). As of December 2025, the second data release for the fifth phase of the SDSS (DR19) was the most comprehensive to date, providing APOGEE spectra and stellar parameters for one million stars (SDSS Collaboration et al. 2025). These stars span a wide range of stellar types, including dwarfs, subgiants, and giants, and are sampled across all major Galactic components: the disk, bulge, and halo.

From the 1,059,521 entries in APOGEE DR19, we selected stars with available internally cross-matched `gaia_dr3_source_id`, and then retained those with `flag_bad` unset to ensure the highest quality of stellar parameters, resulting in 757,338 unique stars identified by their `sdss_id`. For a star with multiple parameter entries due to multi-epoch observations, we calculated the weighted average values and uncertainties for  $T_{\text{eff}}$ ,  $\log g$ , [Fe/H], and  $[\alpha/\text{Fe}]$ , using weights equal to the inverse of the squared parameter uncertainties. Finally, we retained stars with  $T_{\text{eff}} < 8000$  K (see the next section for details) and measurement completeness for all four parameters, resulting in a final sample of 746,853 stars.

### 2.2 Observed photometry from large-volume surveys

Using the `gaia_dr3_source_id` provided in APOGEE DR19, we retrieved photometry for 29 passbands across 7 photometric systems through the crossmatch service from the Gaia archive (Marrese et al. 2019). These 7 photometric systems included *Gaia* DR3 ( $G$ ,  $BP$ ,  $RP$ , Riello et al. 2021), Pan-STARRS DR1 ( $g, r, i, y, z$ , Chambers et al. 2019), APASS DR9 ( $B, V, g, r, i$ , Henden et al. 2016), SkyMapper DR2 ( $u, v, g, r, i, z$ , Onken et al. 2019), SDSS DR13 ( $u, g, r, i, z$ , Alam et al. 2015), 2MASS ( $J, H, K_S$ , Cutri et al. 2003), and ALLWISE ( $W1, W2$ , Cutri et al. 2021)<sup>1</sup>. To detect and remove photometric outliers, such as those caused by flares or saturation, we employed the `SEDEX` pipeline for the SED fitting (Yu et al. 2021, 2023).

The SED fitting was performed in two steps. First, a blackbody distribution was fit to each observed SED under the assumption of zero extinction. This initial fitting was performed iteratively, removing one photometric outlier per iteration until no flux densities deviated from the best-fitting blackbody spectrum by more than 30%. Second, the SED fitting was refined using MARCS synthetic spectra (Gustafsson et al. 2008), constrained by measured  $T_{\text{eff}}$ ,  $\log g$ , and [Fe/H] from APOGEE. Since the maximum  $T_{\text{eff}}$  of the synthetic spectra is 8000 K, we limited our analysis to APOGEE stars with observed  $T_{\text{eff}}$  below this threshold, as mentioned above in section 2.1.

During the second step of the SED fitting process, we calculated the relative difference between the observed flux density in each bandpass and that predicted from the best-fitting model. If the maximum relative difference exceeded 10%, the corresponding photometric measurement was identified as an outlier and rejected. This procedure—removing a single outlier per iteration—was repeated until no further outliers were identified or the remaining data points became too sparse to ensure a reliable fit. Specifically, only those SED fits

with at least 5 valid photometric measurements were retained for subsequent analysis.

Finally, to mitigate remaining photometric outliers in the infrared bands (2MASS and ALLWISE), which are susceptible to noise given their significantly lower fluxes compared to the bluer bands, we further refined the observed SEDs. This involved demanding high-quality 2MASS and ALLWISE photometry by requiring their photometric quality flags (`Qflg`) to be equal to "A". After applying these final quality and  $T_{\text{eff}}$  cuts, our final sample comprised 658,538 stars, of which two thirds were red giants ( $\log g < 3.5$ ).

### 2.3 Synthetic photometry based on Gaia BP/RP spectra

Synthetic magnitudes derived from *Gaia* BP/RP spectra are valuable for this study due to their wide wavelength coverage and inherent homogeneity. These data are available from the *Gaia* archive in the table `gaiadr3.synthetic_photometry_gspc`. To ensure the superior quality of these magnitudes, we applied the following cuts, following Gaia Collaboration et al. (2023b). First, we filtered out stars with potential significant spectral contamination from nearby sources by restricting the corrected color excess parameter  $C^*$  to  $|C^*| < 0.05$  (`gaiadr3.synthetic_photometry_gspc.c_star < 0.05`). Next, we selected synthetic magnitudes only when the associated flux-to-flux error ratio exceeded 30 for the given passbands. This approach meant that, for some red giants, which dominate the APOGEE star sample, synthetic photometry was available for redder filters (higher SNRs) but not for bluer filters (lower SNRs). Finally, we restricted our analysis to synthetic photometry that had been standardized by *Gaia* (Gaia Collaboration et al. 2023b). These systems were Pan-STARRS ( $g, r, i, y, z$ ), SDSS ( $u, g, r, i, z$ ), Johnson-Kron-Cousins ( $U, B, V, R, I$ ), Strömgren ( $v, b, y$ ), and HST ( $F435W, F606W, F814W$ ).

In addition to these standardized sets, we also adopted SkyMapper synthetic photometry; although not formally standardized by *Gaia*, we prioritized these over observed SkyMapper values for two reasons. Firstly, the *Gaia* synthetic catalog provides a significantly larger sample size for our APOGEE stars compared to the available coverage in the SkyMapper Southern Survey (SMSS). More importantly, the SMSS Data Release 4 (DR4)—the latest and final release—is internally calibrated using synthetic magnitudes derived from *Gaia* BP/RP spectra (Onken et al. 2024). Consequently, the extinction coefficients derived in this work are directly applicable to the SkyMapper DR4 photometric system. We note that synthetic SkyMapper  $u$ -band photometry was excluded from this analysis; this is because while the  $v, g, r, i$ , and  $z$  filters are within the *Gaia* BP/RP wavelength range ( $\sim 330$ – $1050$  nm), the  $u$  filter extends down to 300 nm, falling outside the blue-edge limit of the spectra.

While both observed and standardised synthetic photometry were available for the SDSS and Pan-STARRS systems, we prioritized synthetic photometry for these two systems, similarly due to its availability for a larger number of stars. However, observed photometry was still utilized for SED fitting, as incorporating more passbands typically improves the quality of the fit. Consequently, our final dataset included observed photometry for four systems (*Gaia* DR3, APASS DR9, 2MASS, and ALLWISE) and synthetic photometry for six additional systems (Pan-STARRS, SDSS, Johnson-Kron-Cousins, SkyMapper, Strömgren, and HST), providing coverage across 39 filters in total.

<sup>1</sup> ALLWISE W3 and W4 bands were not considered in this work.

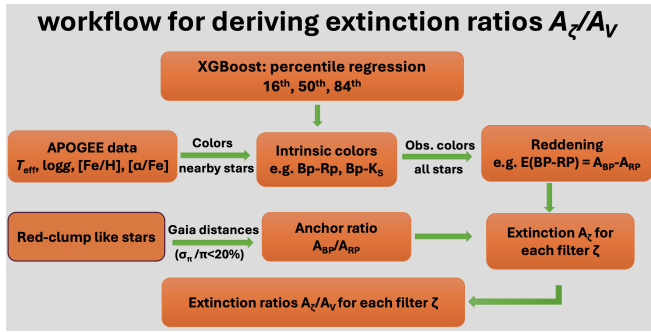


**Figure 1.** Schematic overview of the methodology used to derive extinction ratios  $A_z/A_V$ . Intrinsic colours are inferred from APOGEE stellar parameters using XGBoost quantile regression. Reddening is measured by comparing observed and predicted intrinsic colours, while red-clump-like stars with precise Gaia distances provide an anchor extinction ratio  $A_{BP}/A_{RP}$ , enabling extinction estimates for individual filters and final extinction ratios.

### 3 METHODOLOGY

#### 3.1 Deriving Intrinsic Colors and Reddening

Reddening, or color excess, is formally defined as the difference between observed and intrinsic colors. In this work, observed colors were calculated from either observed or BP/RP inferred synthetic magnitudes, as outlined in Section 2. Intrinsic colors for stars are not directly observable; however, they can be robustly inferred from fundamental stellar parameters ( $T_{\text{eff}}$ ,  $\log g$ ,  $[\text{Fe}/\text{H}]$ , and  $[\alpha/\text{Fe}]$ ) (Chen et al. 2019). To predict intrinsic colors (e.g.,  $(BP - J)_0$ ), we employ XGBoost (eXtreme Gradient Boosting), a machine-learning algorithm well suited for tackling regression tasks with tabular features (Chen & Guestrin 2016). In this model, the input features were  $T_{\text{eff}}$ ,  $\log g$ ,  $[\text{Fe}/\text{H}]$ , and  $[\alpha/\text{Fe}]$ , with values taken from APOGEE DR19. While the contribution of  $[\alpha/\text{Fe}]$  to broadband colors is small, it was included to account for its impact on molecular opacities and line blanketing in cool red giants, which dominate our sample. We found that a 0.5 dex increase in  $[\alpha/\text{Fe}]$ , with all other parameters held fixed, results in an increase of  $\sim 0.03$  mag in the predicted intrinsic  $BP - J$  color. The prediction labels were the intrinsic colors, approximated using stars identified as having negligible extinction. Fig. 1 presents an overview of the methodology to derive reddening and extinction values. Below, we describe the criteria used to identify these low-extinction stars and define the training and validation sets, and then detail the XGBoost training procedure.

##### 3.1.1 Constructing Training, Validation, and Inference sets

The low-extinction stellar sample used for model training and validation was constructed by selecting stars with negligible reddening values,  $E(B - V) < 0.02$ , based on the all-sky two-dimensional dust map of Schlegel et al. (1998) (SFD) as recalibrated by Schlafly & Finkbeiner (2011). To mitigate over-representation of densely populated regions in parameter space (e.g., the red clump), we partitioned the sample into bins in  $T_{\text{eff}}$  and  $[\text{Fe}/\text{H}]$ , using bin sizes of 30 K and 0.2 dex, respectively<sup>2</sup>. Each bin was capped at 300 stars, and bins containing fewer than 15 stars were discarded. A Galactic latitude cut

<sup>2</sup> We also tested binning in  $T_{\text{eff}}$  and  $\log g$ , which yielded inferior performance and was therefore not adopted.

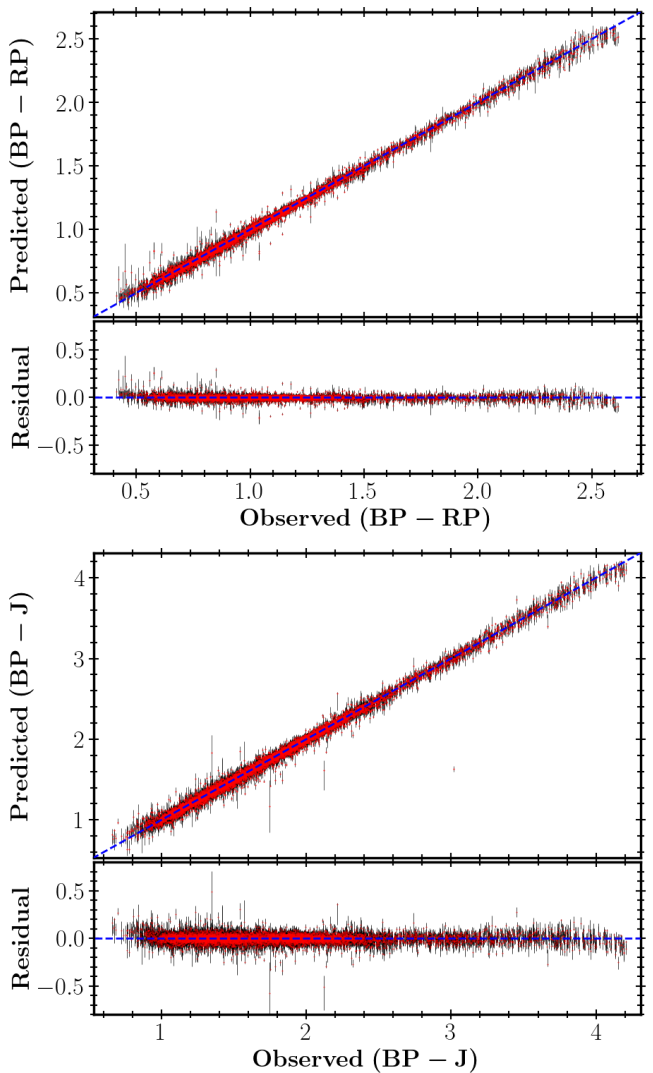


**Figure 2.** Comparison of observed and predicted intrinsic colors for 9126 stars in the validation set with negligible reddening ( $E(B - V)_{\text{SFD}} < 0.02$ ). The top panel shows  $(BP - RP)$ , while the bottom panel displays  $(BP - J)$ . Intrinsic colors are predicted using XGBoost regression models trained on the low-reddening stellar sample. The models utilize  $T_{\text{eff}}$ ,  $\log g$ ,  $[\text{Fe}/\text{H}]$ , and  $[\alpha/\text{Fe}]$  from APOGEE DR19 as input features, with the observed colors of these stars serving as target labels.  $BP$  and  $RP$  magnitudes are retrieved from *Gaia* DR3, and  $J$  magnitudes are from 2MASS. Red points represent the median predicted values, with error bars indicating the  $1\sigma$  uncertainty derived from the 16th and 84th percentiles.

of  $|b| > 10^\circ$  was applied to reduce contamination in both photometry (affecting colors) and spectroscopy (affecting stellar parameters). After applying these cuts, the final low-extinction stellar sample has a mean SFD reddening value of  $E(B - V) = 0.01$ .

The broader sample used for intrinsic color inference comprised all the APOGEE stars in the clean sample that matched the retained bin identifiers of the low-extinction sample, thereby ensuring consistency between the parameter-space coverage used for training and for inference. For model training, 90% of the low-extinction sample was randomly assigned to the training set, while the remaining 10% was reserved for validation. The resulting training set (82,134 stars)

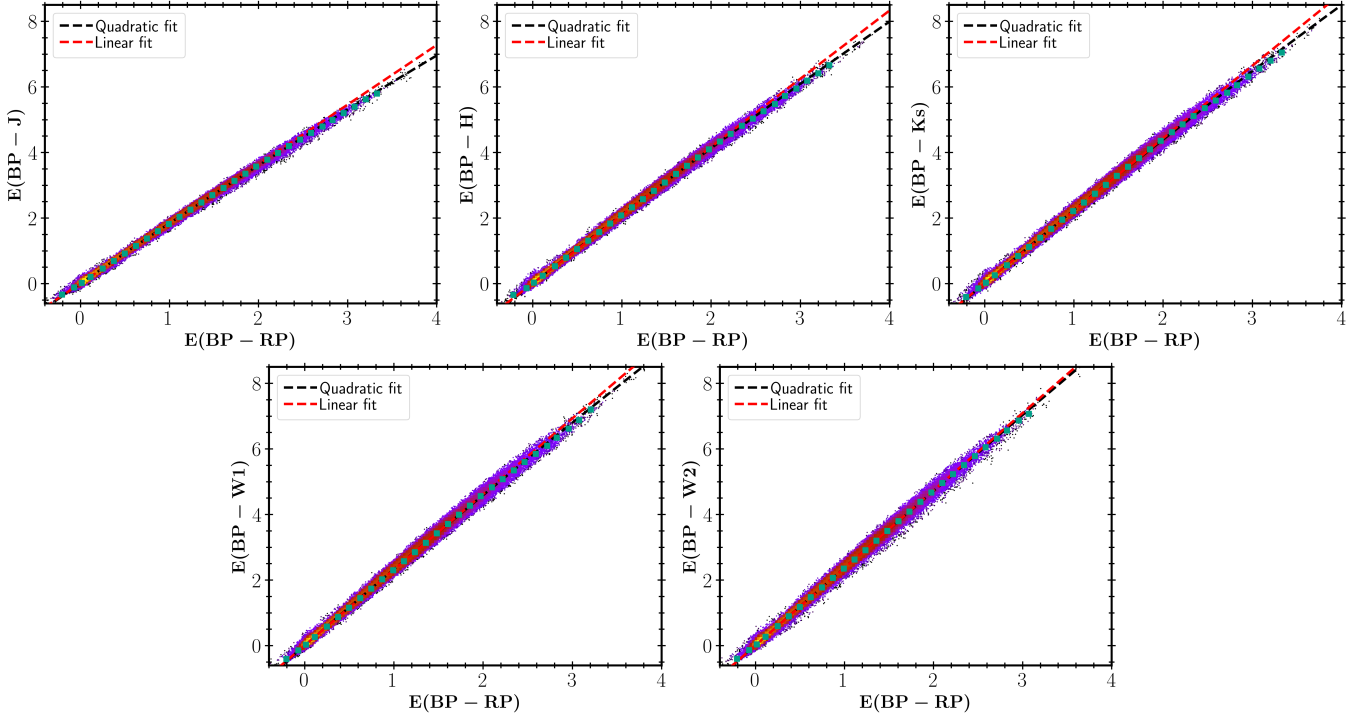


**Figure 3.** Comparison of reddening between  $E(BP - RP)$  and  $E(BP - \zeta)$ , where  $\zeta$  corresponds to various bands. The first row shows 2MASS bands ( $J, H, K_S$ ), and the second row shows WISE bands ( $W1, W2$ ). The black dashed line represents a quadratic fit to the binned averages of the data (green squares; associated standard errors are smaller than the symbol size), while the red dashed line indicates a linear fit to the average values. The density of points is depicted using a color map, with yellow regions indicating higher densities and purple regions representing lower densities.

and validation set (9,126 stars) are sufficiently large to ensure model stability.

Finally, because our primary goal was to derive extinctions for individual filters, we restricted our reddening analysis to 38 colors, rather than all possible colors. This restriction was motivated by the fact that using all 39 available filters would otherwise yield  $39 \times 38/2 = 741$  possible color combinations, which would unnecessarily increase the dimensionality and computational cost of the training. For this, we paired bandpasses by always using one band from *Gaia*  $BP$  or  $RP$  and the other from the remaining 38 filters, denoted  $\zeta$ . The choice between  $BP$  and  $RP$  was determined by which band yielded the largest difference in effective wavelength relative to  $\zeta$  (see Table 1 for effective wavelengths). This was because we found that training performance improved as the wavelength separation between the two bands increased. For example, we used  $u - RP$ , paired from SDSS  $u$  and *Gaia*  $RP$ , and  $BP - J$ , paired from *Gaia*  $BP$  and 2MASS  $J$ .

### 3.1.2 Quantile XGBoost Implementation

Extreme Gradient Boosting (XGBoost) is a robust machine learning algorithm that combines the predictions of an ensemble of decision trees constructed sequentially (Chen & Guestrin 2016). Known for its scalability, efficiency, and strong performance on low-dimensional tabular data, XGBoost is capable of optimizing quantile loss functions and improves model generalization through regularization. Its versatility and effectiveness have been demonstrated in numerous astrophysical applications (e.g. Andrae et al. 2023; Zhang et al. 2024).

In this study, we employed XGBoost for quantile regression to predict the 16<sup>th</sup>, 50<sup>th</sup>, and 84<sup>th</sup> percentiles of intrinsic colors ( $Q_{16}$ ,  $Q_{50}$ , and  $Q_{84}$ , respectively). These percentiles are crucial to capture the distribution of predicted colors and associated uncertainties.

Separate models were trained for each of the 38 colors to ensure precision and flexibility, while maintaining a consistent architecture and hyperparameter configuration across all regressions. The median ( $Q_{50}$ ) was adopted as the final predicted intrinsic color, and the uncertainty ( $\sigma_Q$ ) was calculated as half the interpercentile range:  $\sigma_Q = (Q_{84} - Q_{16})/2$ , where  $Q$  represents a color index.

We used the official package `xgboost` (Chen & Guestrin 2016)<sup>3</sup> with hyperparameters optimized for both accuracy and computational efficiency. The objective was set to ‘`reg:quantileerror`’ to model the desired percentiles, using the root mean square error as the evaluation metric on the validation set. After a thorough grid search, the optimal configuration included 5000 boosting rounds with early stopping at 100 rounds to prevent overfitting. The maximum tree depth was set to 4 to balance model complexity and the capture of non-linear relationships, with a learning rate of 0.03 for stable convergence. To enhance generalization, 80% of features were randomly sampled for each tree. Fig. 2 shows two examples of predicted intrinsic colors for  $BP - RP$  and  $BP - J$ , with median precisions of 0.02 and 0.04 mag, respectively.

Once the intrinsic colors were predicted, the reddening, or color excess  $E(\zeta_1 - \zeta_2)$ , was calculated using the fundamental definition:

$$E(\zeta_1 - \zeta_2) = (\zeta_1 - \zeta_2)_{\text{obs}} - (\zeta_1 - \zeta_2)_{\text{intr}}, \quad (2)$$

where  $(\zeta_1 - \zeta_2)_{\text{obs}}$  and  $(\zeta_1 - \zeta_2)_{\text{intr}}$  are the observed and predicted intrinsic colors, respectively. The uncertainty in  $E(\zeta_1 - \zeta_2)$  was estimated through standard error propagation, considering the uncertainties in both the observed colors (from catalog errors) and the predicted colors ( $\sigma_C$ ).

<sup>3</sup> The package implementation is available at <https://github.com/dmlc/xgboost>

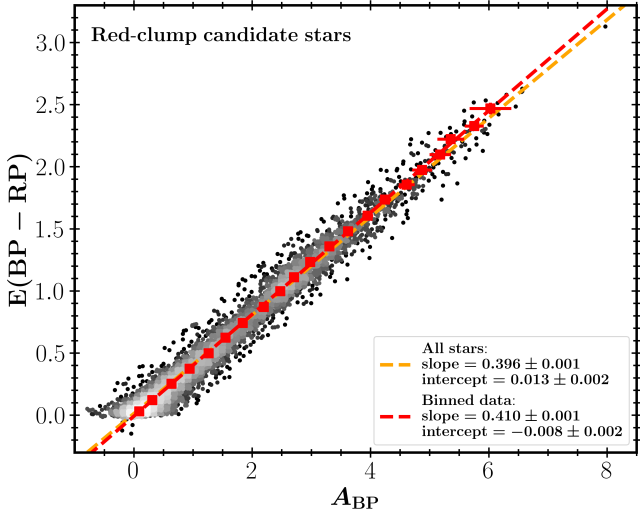


**Figure 4.** Extinction  $A_{BP}$  versus color excess  $E(BP - RP)$  for 8,426 red clump candidate stars (see the text for their selection), color-coded by star number density on a logarithmic scale. The orange dashed line represents the best linear fit (with  $A_{BP}$  as the independent variable) to all the red clump candidate stars, while the red dashed line shows the best linear fit to the mean values binned in color excess  $E(BP - RP)$  with a bin size of 0.12. In both regression models,  $A_{BP}$  was treated as the independent variable and  $E(BP - RP)$  as the dependent variable. The slope and intercept of each best-fit line are annotated in the legend. The  $3\sigma$  outliers w.r.t the orange dashed line, comprising 1.7% of the full sample, are excluded and not shown here.

Fig. 3 illustrates the relationship between  $E(BP - RP)$  and  $E(BP - X)$ , where  $X$  corresponds to various bands (2MASS  $J, H, K_s$  and WISE  $W1, W2$ ). In addition to tight correlations, the comparison reveals a detectable non-linear relationship (curvature) at high reddening values, as indicated by the difference between linear and quadratic fits. Similar curvatures in reddening relationships have been reported in previous studies (e.g., Wang & Chen 2019). This curvature arises from broadband integration effects; as shown in Equation 1, this non-linearity is a function of both the total extinction and  $T_{\text{eff}}$ , which primarily determines the shape of the underlying spectral energy distribution. Consequently, this effect becomes most significant in broader filters and for hotter stars at higher reddening values, where the change in the integrated flux’s centroid (or effective wavelength) is most pronounced.

However, such curvatures do not clearly propagate into the extinction measurements derived from reddening values (as discussed further in Section 5). Deriving extinction from reddening for constructing an extinction curve often involves correcting the broadband extinction  $A_{\zeta}$  to extinction at the passband’s effective wavelength (Wang & Chen 2019). However, this correction introduces a dependence on a pre-existing extinction curve, making the newly derived extinction curve not entirely independent. In this work, we avoided such corrections and instead derived the extinction for individual filters directly. This approach, as we will demonstrate in Section 5, results in extinction ratios that do not exhibit the previously discussed curvature with  $A_V$  even when  $A_V$  reaches up to  $\sim 8$  mag. This means that, by design, our derived extinctions are defined for the integrated response of the full passband, rather than a single effective wavelength.

### 3.2 Deriving Extinction

The overall procedure for deriving extinction for all 39 passbands involved two main steps: first, establishing an accurate extinction ratio ( $A_{BP}/A_{RP}$ ) using Red Clump (RC) like stars, and second, using this anchor point to convert all calculated reddening values into extinctions for individual filters.

We determined the extinction ratio  $A_{BP}/A_{RP}$  by measuring the slope of the linear relationship between the color excess  $E(BP - RP) = A_{BP} - A_{RP}$  and the extinction  $A_{BP}$ . Since  $E(BP - RP)$  was already measured in Section 3.1, this step required the precise estimation of  $A_{BP}$ . For this, we selected a sample of RC-like stars, which are ideal due to their abundance and nearly uniform intrinsic absolute magnitudes (Khanna et al. 2025). The selection criteria, based on APOGEE DR19 stellar parameters, were:  $T_{\text{eff}} = 4750 \pm 100$  K,  $\log g = 2.5 \pm 0.1$  dex, and  $[\text{Fe}/\text{H}] = 0.0 \pm 0.1$  dex.

We determined  $A_{BP}$  through  $A_{BP} = BP - M_{BP} - 5 \log_{10}(d) + 5$ , where  $BP$  is the apparent Gaia magnitude, and the remaining terms give the predicted, reddening-free apparent magnitude of a RC-like star. We derived  $M_{BP}$  from the absolute magnitude in the  $K_s$  band, adopting  $M_{K_s} = -1.650 \pm 0.025$  mag, a well-established value for RC stars from the literature (e.g. Khan et al. 2023). We then used the intrinsic color  $(BP - K_s)_0$  derived from the subset of selected RC-like stars that have negligible calibrated SFD reddening values,  $E(B - V) < 0.02$  (see Section 3.1.1). The median intrinsic color  $(BP - K_s)_0$  for this low-extinction RC sample was found to be  $2.717 \pm 0.053$  mag, yielding an absolute magnitude of  $M_{BP} = (BP - K_s)_0 + M_{K_s} = 1.067 \pm 0.059$  mag. Next, we calculated  $A_{BP}$  for each RC star using  $M_{BP}$ , observed magnitude  $BP$ , and distance  $d$ . We utilized distances from Bailer-Jones et al. (2021) for stars with *Gaia* EDR3 parallax uncertainties better than 20%, prioritizing photo-geometric distances when available, as they are considered more reliable than purely geometric distances Bailer-Jones et al. (2021).

Fig. 4 shows the relationship between  $A_{BP}$  and  $E(BP - RP)$  for the RC-like stars. To derive the extinction ratio  $A_{BP}/A_{RP}$ , we fit a linear model to the binned data in steps of 0.12 mag in  $E(BP - RP)$  (red dashed line, red squares), as we preferred the binned fit to avoid bias due to the overdensity of stars with low extinction (see the grey colormap). The best fit (for the binned data) yielded a slope of  $0.408 \pm 0.001$  and an intercept of  $-0.006 \pm 0.002$ . For comparison, the un-binned data resulted in a slope of  $0.395 \pm 0.001$  and an intercept of  $0.014 \pm 0.002$ . Using the slope derived from the preferred binned linear fit, we calculated the final extinction ratio to be  $A_{BP}/A_{RP} = 1.694 \pm 0.004$ . This value is consistent with previous estimates, such as  $A_{BP}/A_{RP} = 1.686 \pm 0.016$  and  $1.700 \pm 0.007$ , derived in Wang & Chen (2019) using two different methods.

Furthermore, we tested how sensitive this anchor point was to the quality of the adopted parallax. Restricting the RC selection to a parallax precision ( $\sigma_{\varpi}/\varpi$ ) better than 10% (rather than 20%) reduces the sample size from 8,426 to 7,719 stars and shifts  $A_{BP}/A_{RP}$  only slightly, to  $1.700 \pm 0.004$ . This fractional variation of merely 0.3% demonstrates that our adopted anchor point ( $A_{BP}/A_{RP} = 1.694 \pm 0.004$ ) is robust against parallax uncertainties.

Finally, we derived extinctions for all individual passbands using this anchor point,  $A_{BP}/A_{RP} = 1.694 \pm 0.004$ . Combining this ratio with the reddening  $E(BP - RP) = A_{BP} - A_{RP}$ , we calculated the individual extinctions  $A_{BP}$  and  $A_{RP}$  for all stars in the sample. These base extinctions in  $BP$  and  $RP$  then allowed us to calculate the extinction  $A_{\zeta}$  for any other passband  $\zeta$  by utilizing the previously derived reddening values,  $E(BP - \zeta)$  or  $E(\zeta - RP)$ , whichever was used in the XGBoost training (see Section 3.1.1). Notably, this set of  $A_{\zeta}$  includes  $A_V$  for the  $V$  band, which is used in the next Section.

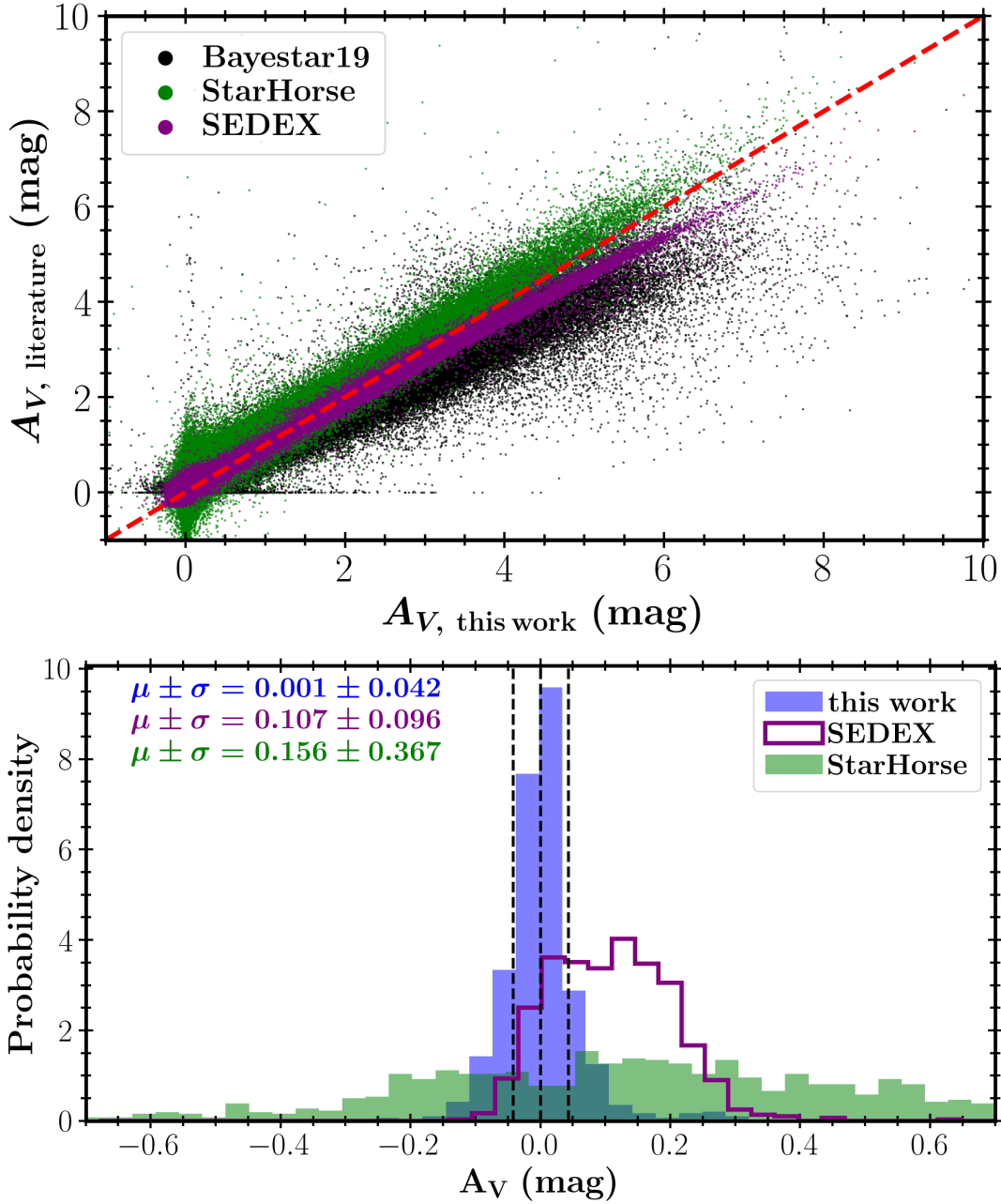


**Figure 5.** Precision and accuracy of our extinction measurements in  $A_V$ . **Upper panel:** Comparison of  $A_V$  values derived in this work with those from Bayestar19 (black), StarHorse (green), and SEDEX (purple). The red dashed line represents the 1:1 relationship. **Lower panel:** Distributions of  $A_V$  derived in this work (blue) compared with those from SEDEX (purple) and StarHorse (green) for nearby stars with distances less than 70 pc. These stars are expected to experience low extinction, making the dispersion of these distributions indicative of the internal  $A_V$  precision. The mean ( $\mu$ ) and  $1\sigma$  uncertainty (calculated from the 16<sup>th</sup> and 84<sup>th</sup> percentiles) are shown in the plot for each method, with results for this work indicated by vertical dashed lines. The  $1\sigma$  dispersion is 0.042 for this work, compared to 0.096 from SEDEX and 0.367 from StarHorse. Negative  $A_V$  values in both panels arise due to measurement uncertainty.

The uncertainties in  $A_{BP}$  and  $A_{RP}$  were derived by propagating the uncertainties in both the anchor ratio  $A_{BP}/A_{RP}$  and the colour excess  $E(BP - RP)$  using standard error-propagation techniques. Likewise, the uncertainties in  $A_\zeta$  were estimated by combining the uncertainties in the corresponding reddening measurements,  $E(BP - \zeta)$  or  $E(\zeta - RP)$ , with the propagated uncertainty in the reference extinction,  $A_{BP}$  or  $A_{RP}$ , depending on which band (i.e.,  $BP$  or  $RP$ ) was adopted as the anchor during the training phase.

Since the anchor ratio  $A_{BP}/A_{RP}$  was calibrated using a sample of

RC-like stars, these extinction measurements are optimised for giant stars, which indeed comprise the majority of our APOGEE sample. We also performed a parallel analysis to derive the  $A_{BP}/A_{RP}$  ratio for various main-sequence populations, binned in  $T_{\text{eff}}$  and  $[\text{Fe}/\text{H}]$  following the same scheme used to define our training and validation sets (see Section 3.1.1). However, the limited number of main-sequence stars—particularly those with high-precision *Gaia* distances—results in substantially lower precision for the derived anchor ratios compared to the RC-like sample. Future data releases with larger samples

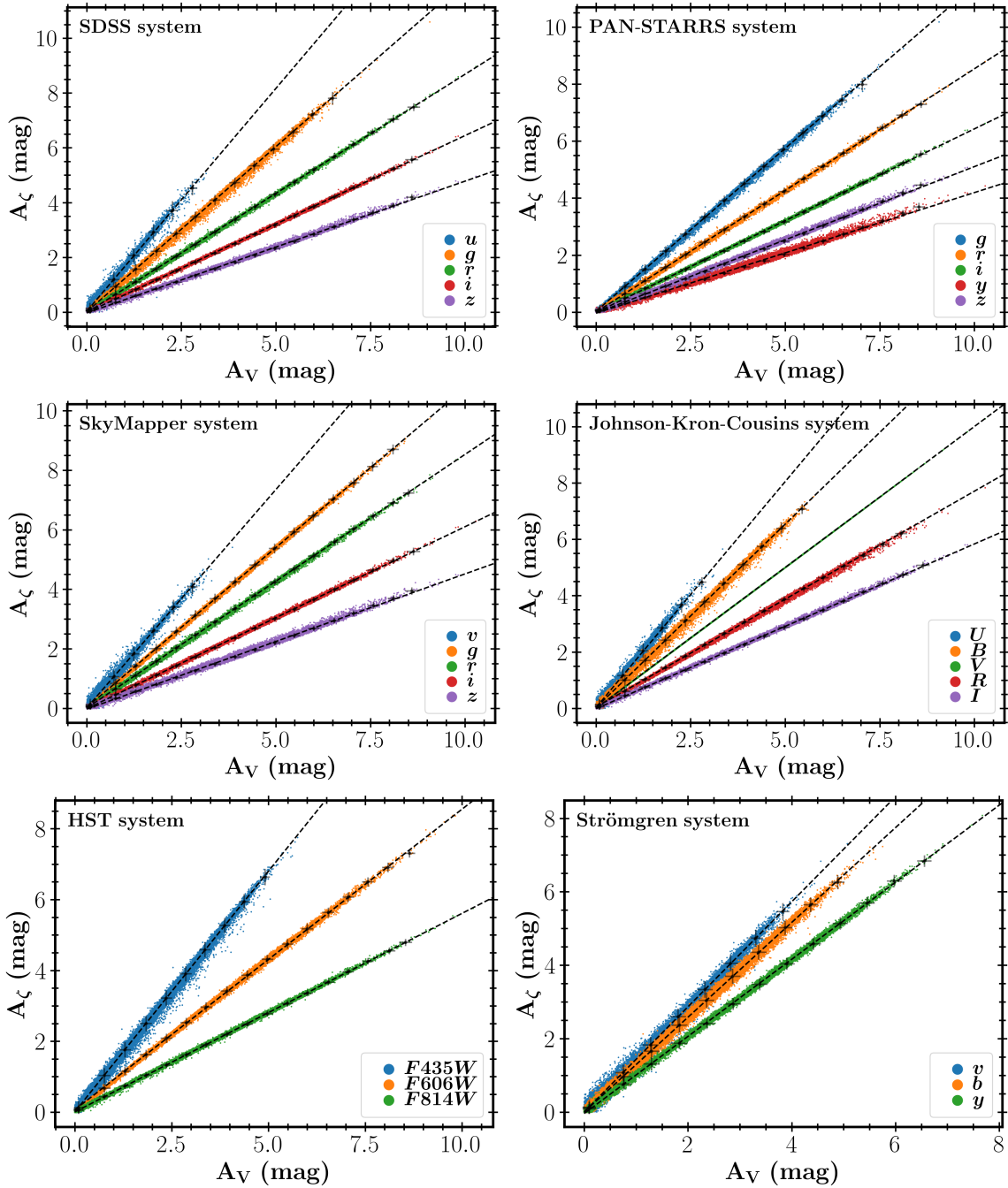


**Figure 6.** Extinction measurements  $A_\zeta$  as a function of  $A_V$  for individual passbands ( $\zeta$ ) within six photometric systems: (a) SDSS, (b) Pan-STARRS, (c) SkyMapper, (d) Johnson-Kron-Cousins, (e) HST, and (f) Strömgren. Synthetic magnitudes derived from Gaia BP/RP spectra are used to calculate these extinctions, considering broader sky coverage compared to associated photometric surveys or observations. With the exception of SkyMapper (see the text for details), only standardized filters by [Gaia Collaboration et al. \(2023b\)](#) are included in this work, which excludes certain filters, such as HST filters different from the three shown here. Each panel displays extinction values derived for individual filters within the respective system, with different colors representing different filters. Large crosses indicate binned averages, while small dots represent individual measurements. Dashed black lines show linear fits used to derive extinction ratios  $A_\zeta/A_V$ . The extinction measurements and their uncertainties are available for download. These data can be used for deriving extinction ratios, extinction-to-reddening ratios, and reddening ratios for user-selected passbands.

of main-sequence stars, especially those with high-precision *Gaia* parallaxes ( $\sigma_\varpi/\varpi < 0.2$ ), will be valuable in refining these ratios across the entire Hertzsprung–Russell diagram.

#### 4 PRECISION AND ACCURACY OF EXTINCTION MEASUREMENTS

In this section, we validate the precision and accuracy of our derived extinction measurements. We compare our results with three established, independent studies: the 3D dust maps of [Bayestar19](#)

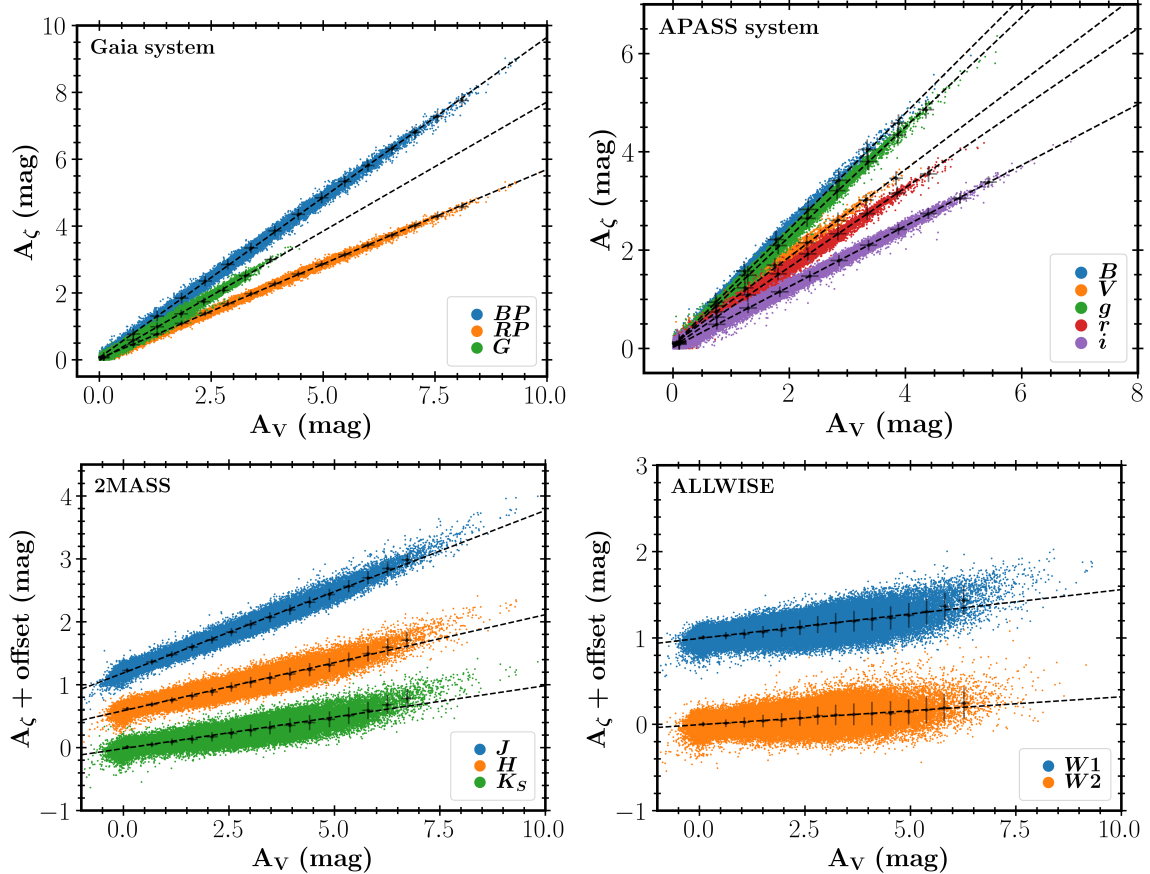


**Figure 7.** Similar to Fig. 6, but now for the following four photometric systems: (a) Gaia, (b) APASS, (c) 2MASS, and (d) ALLWISE, with extinction measurements based on observed photometry. For better visibility, extinction measurements for the  $H$ ,  $K_S$ , and  $W1$  bands are shifted by 0.6, 1.2, and 1.0 mag, respectively. Larger extinction scatter is evident in the 2MASS and ALLWISE filters compared to other filters, due to their lower extinction sensitivity and larger photometric uncertainties. The extinction measurements (not shifted for any bands) and their uncertainties are available for download, while the derived extinction ratios and their uncertainties are provided in Table 1. See Section 5 for why  $A_G$  does not extend to higher values as  $A_{BP}$  and  $A_{RP}$ .

(Green et al. 2019), the StarHorse catalog derived from isochrone fitting (Queiroz et al. 2023), and the SED-based extinctions obtained through the SEDEX pipeline (Yu et al. 2021, 2023). It is important to note the differences in methodology: the  $A_V$  values from Bayestar19 are photometry-based, calculated from their  $E(B-V)$  values assuming  $R_V = 3.1$ . In contrast, the  $A_V$  values derived in this work, as well as those from StarHorse and SEDEX, rely on spectroscopic stellar parameters (from APOGEE DR17 for StarHorse and DR19 for SEDEX).

The upper panel of Fig. 5 demonstrates that, while all methods show general agreement up to  $A_V \approx 8$ , the scatter between them varies significantly. Extinctions derived in this work align closely with those from StarHorse and show the tightest correlation with SEDEX. Conversely, the Bayestar19 values exhibit the largest scatter, particularly at high extinction values. The differences in the scatter are attributed to the differences in the data used: methods relying on spectroscopic data (this work, StarHorse, SEDEX) typically provide higher extinction precision than photometry-based methods (Bayestar19). Regarding the overall accuracy of our measurements, we fitted a linear model comparing our  $A_V$  values with those from the literature. This analysis revealed that our extinction values are globally 17.3% larger than Bayestar19, 11.3% larger than SEDEX, and 3.0% smaller than StarHorse.

We note that the zero point of our extinction measurements, de-

rived using the star-pair method, should be superior to those obtained using StarHorse and SEDEX, by design. If biases exist in the APOGEE stellar parameters, they do not necessarily propagate into our intrinsic color estimates. Because XGBoost is a non-parametric model capable of capturing complex, non-linear dependencies, it can effectively model the systematic biases of stellar parameters as a function of the parameters themselves. As long as these biases remain consistent for stars with similar properties (i.e.,  $T_{\text{eff}}$ ,  $\log g$ ,  $[\text{Fe}/\text{H}]$ , and  $[\alpha/\text{Fe}]$ ) regardless of their sky position, the model implicitly accounts for them during the mapping from observed parameters to intrinsic colors. On the other hand, any biases in the APOGEE stellar parameters can translate into extinction measurements derived from StarHorse and SEDEX because those methods must match observed and model quantities, both of which could introduce biases in the final extinction values. Therefore, based on this robust methodology, we did not correct our extinction scale for subsequent analysis.

The internal precision of our  $A_V$  measurements is assessed from the dispersion of  $A_V$  values for 802 nearby stars ( $d < 70$  pc); this sample lies within the Local Bubble, a region known to have virtually zero reddening (Leroy 1993; Lallement et al. 2014). Because these stars are expected to experience negligible extinction, the dispersion is thus dominated by random noise in the  $A_V$  measurements. The lower panel of Fig. 5 compares the  $A_V$  distributions for this nearby sample derived from this work, StarHorse, and SEDEX. Extinctions

**Table 1.** Extinction ratios,  $A_\zeta/A_V$ , and extinction coefficients,  $A_\zeta/E(B-V)$ , and their uncertainties (see sections 5 and 6 for the methods). A machine-readable version of this table is available via the link provided in the Data Availability section.

Filter	Effective wavelength (Å)	$A_\zeta/A_V$	$\sigma_{A_\zeta/A_V}$	$A_\zeta/E(B-V)$	$\sigma_{A_\zeta/E(B-V)}$	Synthetic magnitude (Yes/No)
APASS <i>B</i>	4299.2	1.179	0.014	3.804	0.045	No
APASS <i>V</i>	5393.9	0.891	0.013	2.869	0.045	No
APASS <i>g</i>	4639.3	1.118	0.008	3.574	0.014	No
APASS <i>r</i>	6122.0	0.810	0.005	2.514	0.016	No
APASS <i>i</i>	7438.9	0.618	0.001	1.945	0.006	No
GAIA <i>BP</i>	5035.8	0.958	0.003	3.110	0.008	No
GAIA <i>RP</i>	7620.0	0.566	0.002	1.836	0.004	No
GAIA <i>G</i>	5822.4	0.773	0.012	2.352	0.027	No
2MASS <i>J</i>	12350.0	0.258	0.002	0.810	0.007	No
2MASS <i>H</i>	16620.0	0.153	0.003	0.478	0.009	No
2MASS <i>K<sub>S</sub></i>	21590.0	0.100	0.004	0.304	0.009	No
WISE <i>W1</i>	33526.0	0.056	0.002	0.186	0.009	No
WISE <i>W2</i>	46028.0	0.032	0.001	0.126	0.008	No
<i>U</i>	3551.1	1.604	0.012	5.172	0.017	Yes
<i>B</i>	4361.9	1.303	0.004	4.149	0.004	Yes
<i>V</i>	5467.6	1.000	0.001	3.146	0.003	Yes
<i>R</i>	6695.8	0.767	0.002	2.464	0.004	Yes
<i>I</i>	8568.9	0.585	0.002	1.811	0.003	Yes
HST <i>F435W</i>	4341.4	1.359	0.003	4.296	0.007	Yes
HST <i>F606W</i>	5776.4	0.849	0.004	2.760	0.006	Yes
HST <i>F814W</i>	8019.7	0.561	0.001	1.767	0.003	Yes
PS1 <i>g</i>	4810.2	1.143	0.003	3.642	0.004	Yes
PS1 <i>r</i>	6155.5	0.854	0.001	2.680	0.003	Yes
PS1 <i>i</i>	7503.0	0.644	0.001	1.998	0.002	Yes
PS1 <i>y</i>	9613.6	0.423	0.004	1.289	0.008	Yes
PS1 <i>z</i>	8668.4	0.514	0.003	1.568	0.005	Yes
SDSS <i>u</i>	3608.0	1.627	0.013	5.211	0.029	Yes
SDSS <i>g</i>	4671.8	1.205	0.002	3.812	0.004	Yes
SDSS <i>r</i>	6141.1	0.870	0.001	2.712	0.003	Yes
SDSS <i>i</i>	7457.9	0.646	0.001	2.005	0.003	Yes
SDSS <i>z</i>	8922.8	0.481	0.003	1.476	0.005	Yes
SkyMapper <i>v</i>	3878.7	1.468	0.006	4.660	0.009	Yes
SkyMapper <i>g</i>	5016.1	1.073	0.002	3.425	0.006	Yes
SkyMapper <i>r</i>	6076.8	0.852	0.001	2.688	0.003	Yes
SkyMapper <i>i</i>	7732.8	0.611	0.001	1.896	0.003	Yes
SkyMapper <i>z</i>	9120.3	0.454	0.003	1.400	0.006	Yes
Strömgren <i>v</i>	4105.3	1.430	0.004	4.433	0.013	Yes
Strömgren <i>b</i>	4693.8	1.291	0.004	4.076	0.006	Yes
Strömgren <i>y</i>	5500.9	1.050	0.004	3.249	0.007	Yes

from this work (blue) exhibit the least scatter among the three methods, yielding a  $1\sigma$  uncertainty of 0.042 mag. This precision is 2.3 times better than that of SEDEX (purple) and 8.7 times better than that of StarHorse (green). Furthermore, the median  $A_V$  from this work is 0.001 mag, which is consistent with the expected negligible extinction for these stars (Leroy 1993; Lallement et al. 2014). Crucially, the median uncertainty of our  $A_V$  measurements (0.03 mag) is consistent with the measured  $A_V$  dispersion (0.042 mag), suggesting that our internal uncertainty estimates are reliable.

## 5 A NEW EXTINCTION CURVE

With our passband extinction measurements for 39 filters, we proceeded to derive extinction ratios for building a new extinction curve. Fig. 6 illustrates the relationship between  $A_V$  and the derived extinction  $A_\zeta$  for 26 filters across six photometric systems: (a) SDSS, (b)

Pan-STARRS, (c) SkyMapper, (d) Johnson-Kron-Cousins, (e) HST, and (f) Strömgren. These extinction measurements were derived from synthetic magnitudes based on *Gaia* BP/RP spectra; with the exception of SkyMapper, all magnitudes were standardized by the *Gaia* collaboration (Gaia Collaboration et al. 2023b).

In Fig. 6, each panel shows the extinction values for individual filters for a given photometric system, revealing strong linear correlations between  $A_V$  and  $A_\zeta$ . That being said, the detectable curvatures previously observed in reddening-to-reddening relationships (which tend toward quadratic at high reddening; see Fig. 3) do not clearly propagate into the extinction-to-extinction relationships, which remain essentially linear. To calculate the extinction ratio  $A_\zeta/A_V$  for each filter  $\zeta$ , we fitted a linear model to the binned averages of  $A_\zeta$  and  $A_V$ , represented by crosses in the figures, while accounting for the standard error in each bin. We find that these ratios show no significant correlation with either  $T_{\text{eff}}$  or  $A_V$ , which is consistent with the

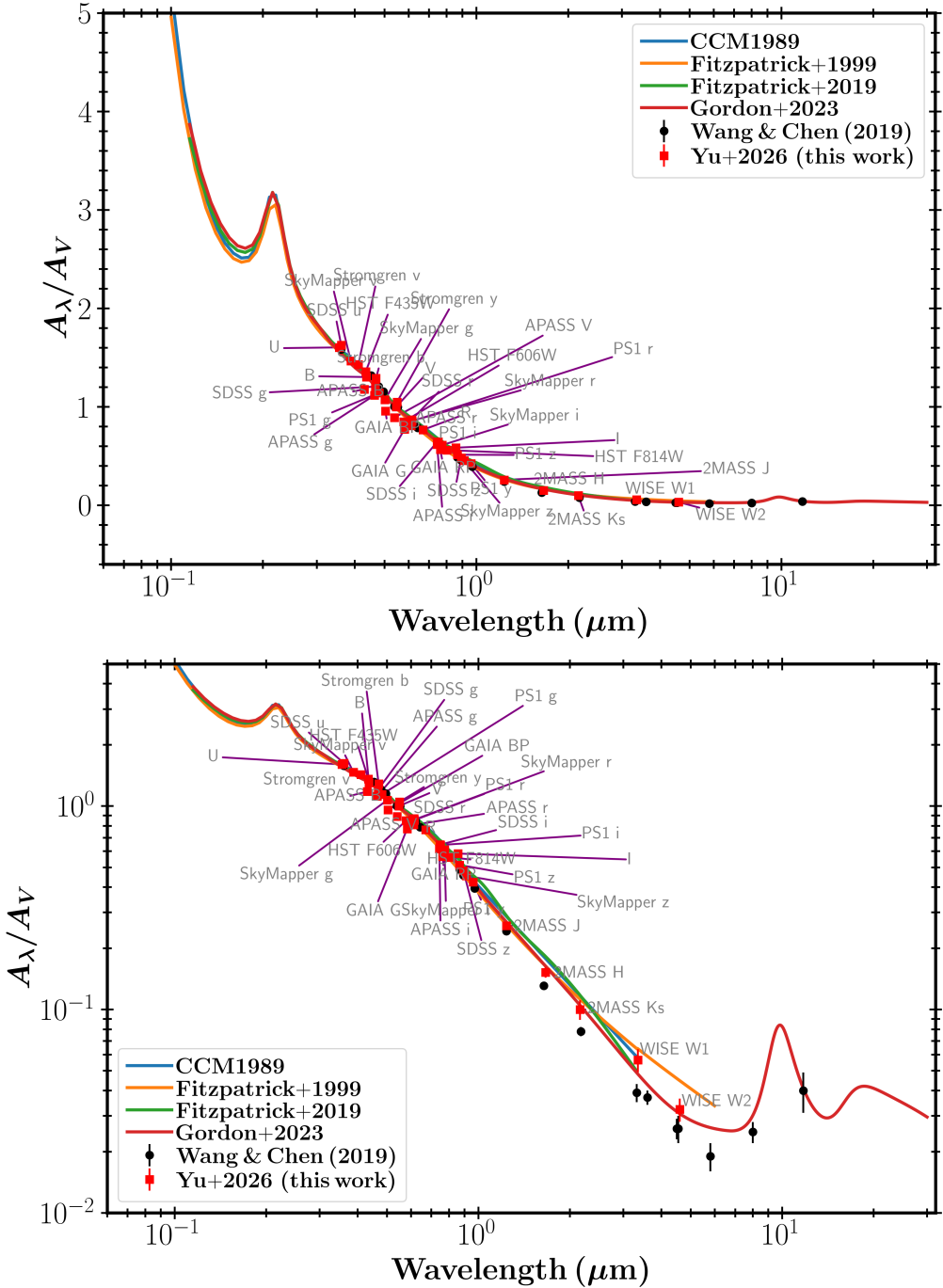


**Figure 8.** A new extinction curve derived in this work, where extinctions ( $A_\lambda$  and  $A_V$ ) are calculated for entire passbands rather than static wavelengths (e.g., effective wavelengths of individual passbands). **Upper panel:** Comparison of the extinction ratios  $A_\lambda/A_V$  derived in this work (red squares) with those from literature extinction curves assuming  $R_V = 3.1$ : Cardelli et al. (1989, blue line), Fitzpatrick (1999, orange line), Fitzpatrick et al. (2019, green line), and Gordon et al. (2023, red line). Black circles represent extinction ratios from Wang & Chen (2019). The extinction ratios derived in this work are shown with their  $3\sigma$  uncertainties, and the extinction values for each filter are labeled. **Lower panel:** Similar to the top panel, but now showing the extinction ratios on a logarithmic scale to better illustrate differences at longer wavelengths.

minimal dispersion observed around the linear trends in Fig. 6. The resulting best-fit extinction ratios and their uncertainties are listed in Table 1.

Extinction measurements for blue filters, such as the SDSS  $u$  band, were available for fewer stars due to our quality cuts on synthetic magnitudes, which required the associated flux-to-flux error ratio to

exceed 30. Because the stars analyzed in this work are predominantly cool red giants, with stars of  $T_{\text{eff}} > 8000$  K excluded, bluer bands like the SDSS  $u$  band were more affected by lower fluxes in these filters, leading to fewer stars meeting the quality criteria.

Similar to the analysis of the synthetic magnitudes for the 6 systems, Fig. 7 presents extinction measurements based on observed

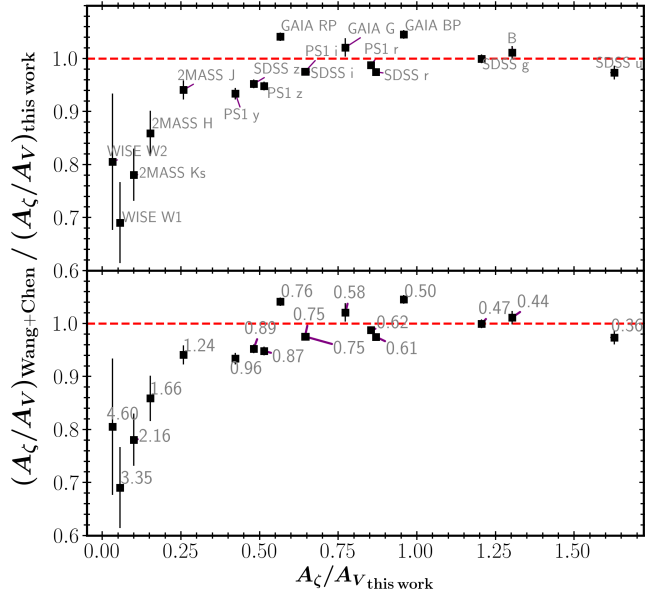


**Figure 9.** Comparison of extinction ratios derived in this work with those from Wang & Chen (2019). **Upper panel:** Each point corresponds to an individual filter, with labels indicating the photometric band. The horizontal dashed line marks a perfect agreement between the two measurements. **Lower panel:** Same ratio as shown above, with numbers indicating the effective wavelengths (in  $\mu\text{m}$ ) of the corresponding filters, adopted from the SVO Filter Profile Service. Deviations from unity increase toward longer wavelengths, particularly in the near- and mid-infrared.

magnitudes for four photometric systems: (a) Gaia, (b) APASS, (c) 2MASS, and (d) ALLWISE. The derived extinction ratios and their associated uncertainties were calculated using the same method and are also provided in Table 1.

We note that extinction measurements for the *Gaia G*-band were systematically unavailable for stars with higher extinction values. This is a consequence of our SED fitting process designed to filter outlier photometry: at high extinction, the monochromatic extinction predicted by a standard extinction curve deviates significantly from the passband-integrated extinction reflected in the observed *G*-band magnitudes (e.g. Casagrande & Vandenberg 2014; Wang & Chen 2019; Zhang & Yuan 2023). Because these measurements appeared as outliers relative to the model, they were removed during the quality-control phase through the SED fitting. Despite this limitation,  $A_G$  still exhibits a clear linear relationship with  $A_V$  when  $A_V \lesssim 4$  mag, suggesting that the differences between monochromatic and passband extinction are negligible in this regime.

Although the APASS photometric system is similar to the Johnson-Kron-Cousins system for the *B* and *V* filters and to the SDSS system for the *g*, *r*, and *i* filters, we still derived extinction ratios specifically for the APASS filters. This approach ensured that the derived extinction ratios aligned with the photometric zero points unique to the APASS system. Extinction measurements for the 2MASS and ALLWISE filters show larger uncertainties compared to other filters. This is primarily due to their lower sensitivity to extinction and higher intrinsic photometric uncertainties, which contributes to the greater scatter observed in their extinction measurements.

Fig. 8 presents the extinction curve derived in this work (39 filters) and compares it with five literature extinction curves assuming  $R_V = 3.1$ : Cardelli et al. (1989), Fitzpatrick (1999), Fitzpatrick et al. (2019), Wang & Chen (2019) and Gordon et al. (2023). Our derived curve

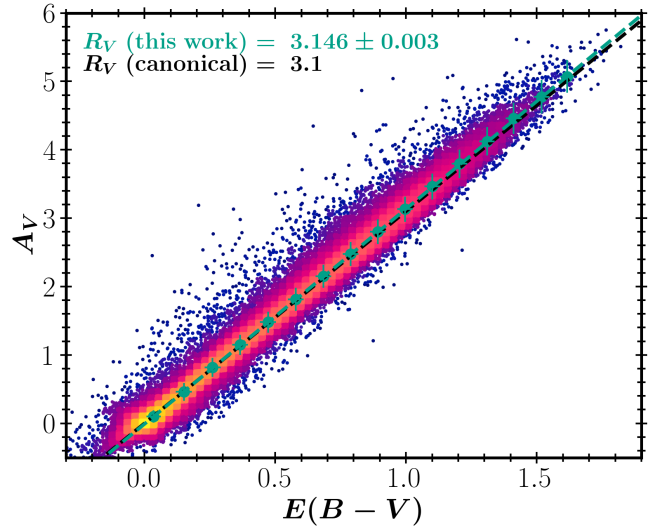


**Figure 10.** Relationship between  $A_V$  and  $E(B - V)$ , color-coded by star number density, with yellow indicating higher density and blue indicating lower density. The green points represent binned averages with their corresponding standard errors. The best-fit relationship, shown by the green dashed line, has a slope of  $R_V = 3.146 \pm 0.003$ , while the canonical relationship with a slope of  $R_V = 3.1$  is indicated by the black dashed line.

exhibits overall consistency with the literature, particularly at shorter wavelengths in the ultraviolet (UV) and optical bands. However, at longer wavelengths, particularly in the infrared (IR) region (e.g., WISE and 2MASS bands), discrepancies become more pronounced, as shown in the lower panel of Fig. 8. Notably, our extinction curve aligns closely with Gordon et al. (2023), but it exhibits systematic differences from Wang & Chen (2019).

Fig. 9 compares our extinction curve with that of Wang & Chen (2019). Overall consistency is observed across optical wavelengths, with most ratios clustering around unity; however, systematic deviations emerge toward longer wavelengths, where Wang & Chen (2019) yield systematically lower extinction ratios. The lower panel shows that this departure from unity increases from wavelengths of  $\sim 700$  nm into the near- and mid-infrared, particularly for the 2MASS and WISE bands. These discrepancies primarily reflect methodological differences: our extinction ratios are derived from passband-integrated measurements using observed and synthetic photometry, whereas Wang & Chen (2019) report extinction ratios evaluated at fixed effective wavelengths. In addition, extinction estimates in the near- and mid-infrared are intrinsically less precise owing to the reduced sensitivity and broader bandpasses of these filters, which further contribute to the observed scatter.

In conclusion, the broadband extinction ratios derived in this work are optimal for correcting extinctions for individual filters, ensuring consistency with passband-integrated observations. Finally, for applications that require the ratios of  $A_\zeta/A_V$  and  $A_\zeta/E(B - V)$  tailored to specific spectral types (e.g., Zhang & Yuan 2023) or evolutionary stages (e.g., Wang et al. 2025a), users can use the extinction measurements provided in our catalog to derive custom ratios beyond the average values reported in Table 1.

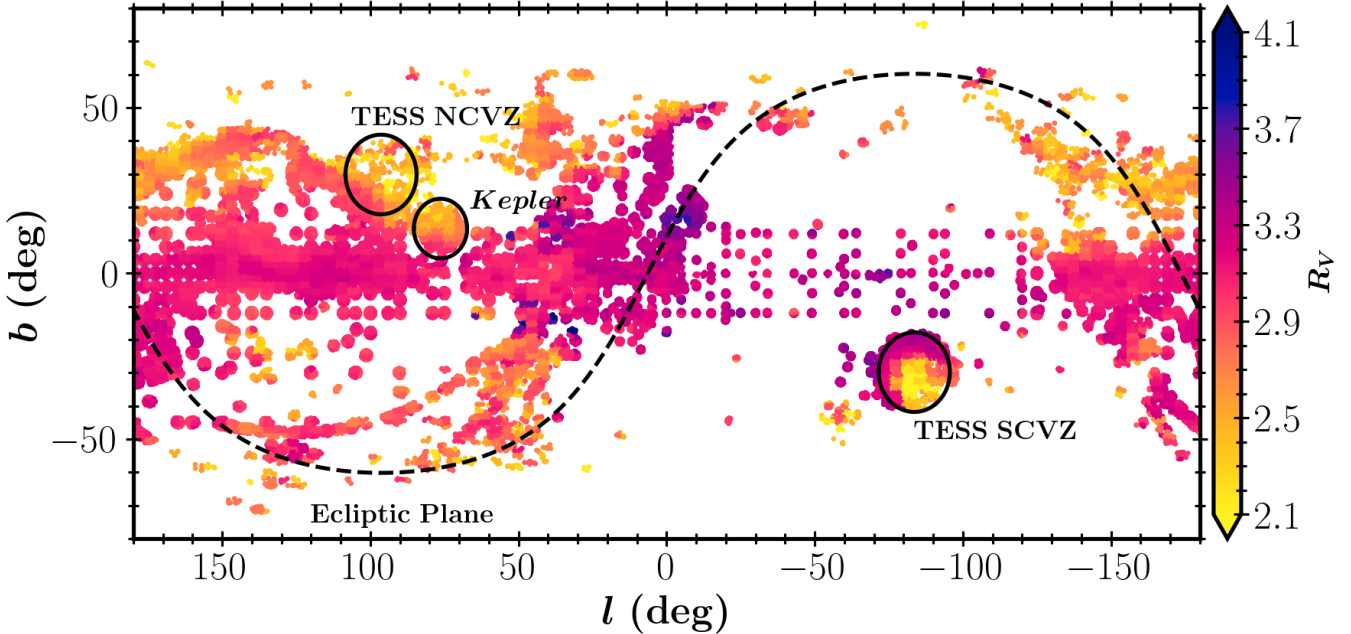


**Figure 11.** Sky map of the extinction coefficient  $R_V = A_V/E(B-V)$  for the APOGEE DR19 footprint in Galactic coordinates ( $l, b$ ). The color bar indicates the average  $R_V$  within each bin, with a resolution of 90 bins in both the  $l$  and  $b$  dimensions. Bins containing fewer than four stars and stars with  $E(B-V) < 0.05$  or  $A_V < 0.1$  are excluded to ensure reliable measurements. The color scale is truncated to the range  $2.1 \leq R_V \leq 4.1$ , corresponding to the interval in which the statistics are well sampled; values outside this range are clipped to the color-bar limits. Within this range, higher  $R_V$  values are predominantly found near the Galactic plane, while lower values are more common at higher Galactic latitudes. The black dashed line denotes the ecliptic plane, along which the  $K2$  fields are situated. The footprints of the *Kepler* field and the TESS northern and southern Continuous Viewing Zones (CVZs) are also indicated, all of which demonstrate significant spatial variations in  $R_V$ .

## 6 EXTINCTION COEFFICIENT $R_V$ ACROSS THE APOGEE DR19 SKY FOOTPRINT

The consistency between our newly derived extinction curve and the literature results suggests that the average  $R_V$  for our stellar sample is  $\sim 3.1$ . To quantify this, we analyzed the relationship between  $A_V$  and  $E(B-V)$  as shown in Fig. 10. A linear fit to the binned averages (represented by green filled circles) yields a slope of  $3.146 \pm 0.003$ , aligning closely with the canonical value of 3.1 (indicated by the black dashed line). Notably, the scatter around this best-fit relation is 0.09 mag, which exceeds our typical  $A_V$  uncertainty of 0.03 mag. This discrepancy implies that the observed dispersion is driven by intrinsic variations in the extinction curve rather than random measurement errors.

It is well established that such variations in  $R_V$  can be typically attributed to differences in dust grain size distributions, chemical compositions, and local radiation environments (Schlafly et al. 2016; Green et al. 2019; Zhang et al. 2023). Fig. 11 illustrates the spatial distribution of the extinction coefficient  $R_V = A_V/E(B-V)$  across the APOGEE DR19 footprint. We observe that higher  $R_V$  values ( $\sim 4.1$ ) are predominantly concentrated near the Galactic plane, whereas lower values ( $\sim 2.1$ ) characterize the higher Galactic latitudes. It is noteworthy that the large variation of  $R_V$  suggests that the initial photometric filtering—which relied on SED fitting as detailed in Section 2.2—does not significantly bias the sample by removing stars located behind “non-standard” dust. The spatial trends we see are in agreement with previous studies (e.g., Schlafly et al. 2016; Zhang et al. 2023; Zhang & Green 2025; Green et al. 2025).

The observed spatial gradient in  $R_V$  reflects the heterogeneous physical conditions of the interstellar medium (ISM, Draine 2003).

The higher  $R_V$  values found within the Galactic plane point to environments dominated by larger dust grains, a characteristic feature of the dense molecular clouds associated with active star formation. In these high-density regions, processes such as grain coagulation and mantle accretion facilitate the growth of larger particles, thereby increasing  $R_V$  (Ossenkopf 1993). In contrast, the lower  $R_V$  values observed at higher latitudes are indicative of the diffuse ISM. In these less-shielded, lower-density environments, small grains are more prevalent due to fragmentation from interstellar shocks or erosion by the interstellar radiation field (Jones et al. 1996).

The spatial distribution of  $R_V$  across key space-mission footprints—namely the *Kepler* field and the TESS northern and southern Continuous Viewing Zones (CVZs)—exhibits pronounced small-scale variations that have important implications for precision stellar astrophysics. These regions are prioritized for long-duration photometric monitoring to enable exoplanet characterization and asteroseismic analysis. Our results reveal that  $R_V$  is markedly non-uniform across all three fields (with stars in the Large Magellanic Cloud removed), reflecting the intrinsically inhomogeneous structure of the intervening interstellar medium. Such spatial variations in  $R_V$  can introduce significant systematic biases in fundamental stellar parameters, including luminosities and radii, when *Gaia* parallaxes are combined with broadband photometry under the assumption of a standard Galactic average ( $R_V = 3.1$ ). Therefore, accurate, position-dependent  $R_V$  corrections are essential for achieving the precision required in modern stellar studies.

In addition to  $R_V$ , we derived extinction coefficients (i.e., total-to-selective extinction ratios),  $A_\zeta/E(B-V)$ , for additional 38 filters using the same linear regression method employed for  $R_V$ . These

measured coefficients, along with their respective uncertainties, are detailed in Table 1. This suite of coefficients provides a toolset for applying extinction corrections across a broad range of photometric systems, particularly when utilizing reddening values (e.g.,  $E(B-V)$ ) derived from 3D dust maps. In addition, our publicly available reddening measurements enable users to derive reddening ratios for arbitrary colour combinations among the 39 filters considered (e.g.,  $E(BP-RP)/E(B-V)$ ).

## 7 CONCLUSION

High-precision reddening and extinction measurements are of fundamental importance to a wide range of stellar and interstellar studies. In particular, they are essential for applying accurate extinction corrections when deriving precise stellar parameters from *Gaia* parallaxes. The primary objective of this study was to establish a high-fidelity catalog of reddening and extinction measurements for the APOGEE DR19 stars. Using these data, we derived extinction ratios ( $A_\zeta/A_V$ ) and extinction coefficients ( $A_\zeta/E(B-V)$ ) specifically optimized for broadband photometry.

To achieve this, we leveraged high-quality spectroscopic parameters from APOGEE DR19 and standardized synthetic magnitudes from *Gaia* BP/RP spectra to estimate intrinsic colors. This was accomplished using an XGBoost regression model trained on a sample of stars with negligible reddening ( $E(B-V)_{\text{SFD}} < 0.02$ ). By comparing these predicted intrinsic colors with observed measurements, we derived precise reddening values. These color excesses were subsequently converted into absolute extinctions, anchored by a precisely determined ratio of  $A_{BP}/A_{RP} = 1.694 \pm 0.004$  obtained from a sample of RC-like stars (Fig. 4).

The resulting catalog provides high-fidelity extinction and reddening estimates for 39 filters across 10 distinct photometric systems (publicly available for download at <https://doi.org/10.5281/zenodo.1823958>). This catalog enables the derivation of precise extinction ratios ( $A_\zeta/A_V$ ), extinction-to-reddening ratios ( $A_\zeta/E(B-V)$ ), and reddening ratios (e.g.,  $E(BP-RP)/E(B-V)$ ) for any combination of the following passbands:

- **Gaia:**  $G, BP, RP$
- **Pan-STARRS1:**  $g, r, i, z, y$
- **SDSS:**  $u, g, r, i, z$
- **APASS:**  $B, V, g, r, i$
- **Johnson-Kron-Cousins:**  $U, B, V, R, I$
- **SkyMapper:**  $v, g, r, i, z$
- **Strömgren:**  $v, b, y$
- **HST:**  $F435W, F606W, F814W$
- **2MASS:**  $J, H, K_S$
- **ALLWISE:**  $W1, W2$

Compared with extinction measurements from existing catalogs and methods—namely Bayestar19 (Green et al. 2019), StarHorse (Queiroz et al. 2023), and SEDEX (Yu et al. 2021, 2023)—our results demonstrate superior precision, achieving a typical  $A_V$  uncertainty of  $\sim 0.03$  mag. The newly derived extinction curve shows good agreement with established literature (Cardelli et al. 1989; Fitzpatrick 1999; Fitzpatrick et al. 2019; Gordon et al. 2023; Wang & Chen 2019) at shorter wavelengths in the UV and optical regimes (Fig. 8). However, notable discrepancies emerge at longer wavelengths ( $\lambda > 700$  nm), particularly in the near- and mid-infrared (e.g., 2MASS and *WISE* bands). These differences likely arise from the varying treatments of extinction ratios across studies—specifically the distinction between broadband-integrated and monochromatic

ratios. While the newly derived extinction curve characterizes an average  $R_V = 3.146 \pm 0.003$  (Fig. 10), we resolve significant spatial variations in  $R_V$ , with higher values concentrated near the Galactic plane and lower values at higher Galactic latitudes (Fig. 11).

The methodology developed in this work has yielded a precise reddening and extinction catalog that will serve as a foundation for several future applications. As part of a forthcoming series of studies, the superior precision of these measurements will enable a revision of the  $v_{\text{max}}$  asteroseismic scaling relation (Hekker 2020) and provide critical anchor points for the absolute calibration of differential reddening in open clusters (Kalup & Molnár 2026), leading to more reliable age determinations via isochrone fitting. Furthermore, by exploiting these high-precision measurements across an extensive number of lines of sight, our results offer a robust mechanism to reconcile existing heterogeneous dust maps (e.g., Drimmel et al. 2003; Marshall et al. 2006; Sale et al. 2014; Green et al. 2019; Lallement et al. 2022; Wang et al. 2025b) into a single, all-sky homogeneous extinction model. This unified framework will provide a consistent view of the dust distribution within the Milky Way, facilitating more accurate studies of Galactic structure and stellar populations.

## ACKNOWLEDGEMENTS

RD is supported in part by the Italian Space Agency (ASI) through contract 2025-10-HH.0 to the National Institute for Astrophysics (INAF). D.S. is supported by the Australian Research Council (DP250104267). SK acknowledges support from the European Union’s Horizon 2020 research and innovation program under the GaiaUnlimited project (grant agreement No 101004110).

Funding for the Sloan Digital Sky Survey V has been provided by the Alfred P. Sloan Foundation, the Heising-Simons Foundation, the National Science Foundation, and the Participating Institutions. SDSS acknowledges support and resources from the Center for High-Performance Computing at the University of Utah. SDSS telescopes are located at Apache Point Observatory, funded by the Astrophysical Research Consortium and operated by New Mexico State University, and at Las Campanas Observatory, operated by the Carnegie Institution for Science. The SDSS web site is [www.sdss.org](http://www.sdss.org).

SDSS is managed by the Astrophysical Research Consortium for the Participating Institutions of the SDSS Collaboration, including the Carnegie Institution for Science, Chilean National Time Allocation Committee (CNTAC) ratified researchers, Caltech, the Gotham Participation Group, Harvard University, Heidelberg University, The Flatiron Institute, The Johns Hopkins University, L’Ecole polytechnique fédérale de Lausanne (EPFL), Leibniz-Institut für Astrophysik Potsdam (AIP), Max-Planck-Institut für Astronomie (MPIA Heidelberg), Max-Planck-Institut für Extraterrestrische Physik (MPE), Nanjing University, National Astronomical Observatories of China (NAOC), New Mexico State University, The Ohio State University, Pennsylvania State University, Smithsonian Astrophysical Observatory, Space Telescope Science Institute (STScI), the Stellar Astrophysics Participation Group, Universidad Nacional Autónoma de México, University of Arizona, University of Colorado Boulder, University of Illinois at Urbana-Champaign, University of Toronto, University of Utah, University of Virginia, Yale University, and Yunnan University.

This work made use of data from ESA’s *Gaia* mission, processed by the *Gaia* Data Processing and Analysis Consortium (DPAC). DPAC is funded by national institutions participating in the *Gaia* Multilateral Agreement.

This work made use of the Overleaf platform and the NASA Astrophysics Data System.

## DATA AVAILABILITY

Reddening and extinction measurements derived in this work, along with their associated uncertainties, are available for download at <https://doi.org/10.5281/zenodo.18239586>. The extinction ratios ( $A_{\zeta}/A_V$ ) and coefficients ( $A_{\zeta}/E(B-V)$ ) summarized in Table 1 are also included in the machine-readable files provided at the same repository.

## REFERENCES

Alam S., et al., 2015, *The Astrophysical Journal Supplement Series*, 219, 12  
 Andrae R., Rix H.-W., Chandra V., 2023, *The Astrophysical Journal Supplement Series*, 267, 8  
 Bailer-Jones C. A. L., Rybizki J., Fouesneau M., Demleitner M., Andrae R., 2021, *The Astronomical Journal*, 161, 147  
 Brown T. M., Gilliland R. L., Noyes R. W., Ramsey L. W., 1991, *The Astrophysical Journal*, 368, 599  
 Cardelli J. A., Clayton G. C., Mathis J. S., 1989, *The Astrophysical Journal*, 345, 245  
 Casagrande L., Vandenberg D. A., 2014, *Monthly Notices of the Royal Astronomical Society*, 444, 392  
 Chambers K. C., et al., 2019, *The Pan-STARRS1 Surveys* ([arXiv:1612.05560](https://arxiv.org/abs/1612.05560)), doi:10.48550/arXiv.1612.05560  
 Chen T., Guestrin C., 2016, XGBoost: A Scalable Tree Boosting System, doi:10.48550/arXiv.1603.02754  
 Chen B.-Q., et al., 2019, *Monthly Notices of the Royal Astronomical Society*, 483, 4277  
 Cutri R. M., et al., 2003, VizieR Online Data Catalog, 2246, II/246  
 Cutri R. M., et al., 2021, VizieR Online Data Catalog, p. II/328  
 De Angeli F., et al., 2023, *Astronomy & Astrophysics*, 674, A2  
 Decleir M., et al., 2022, *The Astrophysical Journal*, 930, 15  
 Draine B. T., 2003, *Annual Review of Astronomy and Astrophysics*, 41, 241  
 Drimmel R., Cabrera-Lavers A., López-Corredoira M., 2003, *Astronomy & Astrophysics*, 409, 205  
 Drimmel R., Skowron D. M., Khanna S., Poggio E., Fouesneau M., 2026, in prep.  
 Fitzpatrick E. L., 1999, *Publications of the Astronomical Society of the Pacific*, 111, 63  
 Fitzpatrick E. L., Massa D., Gordon K. D., Bohlin R., Clayton G. C., 2019, *The Astrophysical Journal*, 886, 108  
 Gaia Collaboration et al., 2023a, *Astronomy & Astrophysics*, 674, A1  
 Gaia Collaboration et al., 2023b, *Astronomy & Astrophysics*, 674, A33  
 Gordon K. D., Cartledge S., Clayton G. C., 2009, *The Astrophysical Journal*, 705, 1320  
 Gordon K. D., et al., 2021, *The Astrophysical Journal*, 916, 33  
 Gordon K. D., Clayton G. C., Decleir M., Fitzpatrick E. L., Massa D., Misselt K. A., Tollerud E. J., 2023, *The Astrophysical Journal*, 950, 86  
 Green G. M., Schlafly E., Zucker C., Speagle J. S., Finkbeiner D., 2019, *The Astrophysical Journal*, 887, 93  
 Green G. M., Zhang X., Zhang R., 2025, *The Astrophysical Journal*, 988, 5  
 Gustafsson B., Edvardsson B., Eriksson K., Jørgensen U. G., Nordlund Å., Plez B., 2008, *Astronomy & Astrophysics*, 486, 951  
 Hekker S., 2020, *Frontiers in Astronomy and Space Sciences*, 7, 3  
 Henden A. A., Templeton M., Terrell D., Smith T. C., Levine S., Welch D., 2016, VizieR Online Data Catalog, 2336, II/336  
 Huang B., et al., 2024, *The Astrophysical Journal Supplement Series*, 271, 13  
 Jones A. P., Tielens A. G. G. M., Hollenbach D. J., 1996, *The Astrophysical Journal*, 469, 740  
 Kalup C., Molnár L., 2026, *The Astronomical Journal*, 171, 45  
 Khan S., Anderson R. I., Miglio A., Mosser B., Elsworth Y. P., 2023, *Astronomy & Astrophysics*, 680, A105  
 Khanna S., et al., 2025, *Astronomy & Astrophysics*, 701, A270  
 Kjeldsen H., Bedding T. R., 1995, *Astronomy & Astrophysics*, 293, 87  
 Lallement R., Vergely J.-L., Valette B., Puspitarini L., Eyer L., Casagrande L., 2014, *Astronomy and Astrophysics*, 561, A91  
 Lallement R., Vergely J. L., Babusiaux C., Cox N. L. J., 2022, *Astronomy & Astrophysics*, 661, A147  
 Leroy J. L., 1993, *Astronomy & Astrophysics*, 274, 203  
 Lindegren L., et al., 2021, *Astronomy & Astrophysics*, 649, A4  
 Majewski S. R., et al., 2017, *The Astronomical Journal*, 154, 94  
 Marrese P. M., Marinoni S., Fabrizio M., Altavilla G., 2019, *Astronomy & Astrophysics*, 621, A144  
 Marshall D. J., Robin A. C., Reylé C., Schultheis M., Picaud S., 2006, *Astronomy & Astrophysics*, 453, 635  
 Massa D., Savage B. D., Fitzpatrick E. L., 1983, *The Astrophysical Journal*, 266, 662  
 Mészáros S., et al., 2025, *The Astronomical Journal*, 170, 96  
 Montegriffo P., et al., 2023, *Astronomy & Astrophysics*, 674, A3  
 Onken C. A., et al., 2019, *Publications of the Astronomical Society of Australia*, 36, e033  
 Onken C. A., Wolf C., Bessell M. S., Chang S.-W., Luval L. C., Tonry J. L., White M. C., Da Costa G. S., 2024, *Publications of the Astronomical Society of Australia*, 41, e061  
 Ossenkopf V., 1993, *Astronomy & Astrophysics*, 280, 617  
 Peek J. E. G., Schiminovich D., 2013, *The Astrophysical Journal*, 771, 68  
 Queiroz A. B. A., et al., 2023, *Astronomy & Astrophysics*, 673, A155  
 Riello M., et al., 2021, *Astronomy & Astrophysics*, 649, A3  
 Rodrigues T. S., et al., 2014, *Monthly Notices of the Royal Astronomical Society*, 445, 2758  
 SDSS Collaboration et al., 2025, The Nineteenth Data Release of the Sloan Digital Sky Survey, doi:10.48550/arXiv.2507.07093  
 Sale S. E., et al., 2014, *Monthly Notices of the Royal Astronomical Society*, 443, 2907  
 Schlafly E. F., Finkbeiner D. P., 2011, *The Astrophysical Journal*, 737, 103  
 Schlafly E. F., et al., 2016, *The Astrophysical Journal*, 821, 78  
 Schlegel D. J., Finkbeiner D. P., Davis M., 1998, *The Astrophysical Journal*, 500, 525  
 Stecher T. P., 1965, *The Astrophysical Journal*, 142, 1683  
 Ulrich R. K., 1986, *The Astrophysical Journal Letters*, 306, L37  
 Wang S., Chen X., 2019, *The Astrophysical Journal*, 877, 116  
 Wang H., Chen X., Wang S., 2025a, The Dependence of the Extinction Coefficient on Reddening for Galactic Cepheids ([arXiv:2512.23311](https://arxiv.org/abs/2512.23311)), doi:10.48550/arXiv.2512.23311  
 Wang T., et al., 2025b, *The Astrophysical Journal Supplement Series*, 280, 15  
 Wilson J. C., et al., 2019, *Publications of the Astronomical Society of the Pacific*, 131, 055001  
 Yu J., Huber D., Bedding T. R., Stello D., Murphy S. J., Xiang M., Bi S., Li T., 2016, *Monthly Notices of the Royal Astronomical Society*, 463, 1297  
 Yu J., Bedding T. R., Stello D., Huber D., Compton D. L., Gizon L., Hekker S., 2020, *Monthly Notices of the Royal Astronomical Society*, 493, 1388  
 Yu J., Hekker S., Bedding T. R., Stello D., Huber D., Gizon L., Khanna S., Bi S., 2021, *Monthly Notices of the Royal Astronomical Society*, 501, 5135  
 Yu J., Khanna S., Themessl N., Hekker S., Dréau G., Gizon L., Bi S., 2023, *The Astrophysical Journal Supplement Series*, 264, 41  
 Yuan H. B., Liu X. W., Xiang M. S., 2013, *Monthly Notices of the Royal Astronomical Society*, 430, 2188  
 Zhang X., Green G. M., 2025, *Science*, 387, 1209  
 Zhang R., Yuan H., 2023, *The Astrophysical Journal Supplement Series*, 264, 14  
 Zhang R., Yuan H., Chen B., 2023, *The Astrophysical Journal Supplement Series*, 269, 6  
 Zhang J., et al., 2024, *The Astrophysical Journal Supplement Series*, 272, 40

This paper has been typeset from a  $\text{\TeX}/\text{\LaTeX}$  file prepared by the author.